Transition to turbulence in rotating-disk boundary layers—convective and absolute instabilities

**Thomas C. Corke · Eric H. Matlis ·
Hesham Othman**

Abstract This work is an experimental study of mechanisms for transition to turbulence in the boundary layer on a rotating disk. In one case, the focus was on a triad resonance between pairs of traveling cross-flow modes and a stationary cross-flow mode. The other was on the temporal growth of traveling modes through a linear absolute instability mechanism first discovered by Lingwood (1995, J Fluid Mech 314:373–405). Both research directions made use of methods for introducing controlled initial disturbances. One used a distributed array of ink dots placed on the disk surface to enhance a narrow band of azimuthal and radial wave numbers of both stationary and traveling modes. The size of the dots was small so that the disturbances they produce were linear. Another approach introduced temporal disturbances by a short-duration air pulse from a hypodermic tube located above the disk and outside the boundary layer. Hot-wire sensors primarily sensitive to the azimuthal velocity component, were positioned at different spatial (r, θ) locations on the disk to document the growth of disturbances. Spatial correlation measurements were used with two simultaneous sensors to obtain wavenumber vectors. Cross-bicoherence was used to identify three-frequency phase locking. Ensemble averages conditioned on the air pulses revealed wave packets that evolved in time and space. The space–time evolution of the leading and trailing edges of the wave packets were followed past the critical radius for the absolute instability, r_{c_A}. With documented linear amplitudes, the spreading of the disturbance wave packets did not continue to grow in time as r_{c_A} was approached. Rather, the spreading of the trailing edge of the wave packet decelerated and asymptotically approached a constant. This result supports the linear DNS simulations of Davies and Carpenter (2003, J Fluid Mech 486:287–329) who concluded that the absolute instability mechanism does not result in a global mode, and that linear-disturbance wave packets are dominated by the convective instability. In contrast, wave-number matching between traveling cross-flow modes confirmed a triad resonance that lead to the growth of a low azimuthal number ($n = 4$) stationary mode. At transition, this mode had the largest amplitude. Signs of this mechanism can be found in past flow visualization of transition to turbulence in rotating disk flows.

Keywords Absolute instability · Cross-flow instability · Rotating-disk boundary layer

T. C. Corke (✉) · E. H. Matlis · H. Othman
Department of Aerospace and Mechanical Engineering, Center for Flow Physics and Control, University of Notre Dame, Notre Dame, IN 46556, USA
e-mail: tcorke@nd.edu

1 Introduction

The boundary-layer flow over a rotating disk in a quiescent fluid has frequently been used as a canonical three-dimensional flow which exemplifies the cross-flow instability. In this flow, the instability appears as outward-spiraling waves. These were first detected experimentally in the hot-wire measurements of Smith [1]. The theoretical analysis accompanying experimental results followed later in the classic paper by Gregory, Stuart and Walker [2]. In that they surmised a number of key elements about this instability such as the role small surface roughness could have in fixing the locations of stationary modes, and the expected existence of traveling modes which could not be detected in their surface-flow visualization.

Even though linear theory predicts the traveling modes to be more amplified, a majority of the experiments have focused on stationary cross-flow modes. The reasons for this are twofold. The first is that many of the studies have been based on flow visualization [2–5] which tends to emphasize stationary components. The second is the sensitivity of this instability to surface roughness which can bias the larger-amplitude modes towards the stationary type. For example, Wilkinson and Malik [6] observed that stationary modes originated from exceedingly small randomly placed dust particles on the surface of a "clean" disk. This prompted them to study the effect of a single isolated surface roughness. From this they observed the growth of wave packets which rapidly spread around the disk to eventually fill the entire circumference.

The simultaneous existence of stationary and traveling cross-flow modes of comparable amplitudes opens the possibility of a nonlinear interaction between them. Lekoudis [7] was one of the first to consider the possibility of a triad-type interaction between traveling cross-flow waves in the three-dimensional boundary layer on a swept wing. For the same flow, Malik et al. [8] used a nonlinear model to study the interaction between traveling and stationary cross-flow modes. They considered only "tuned" resonance cases with a pair of traveling modes with the same frequency and equal–opposite spanwise wave numbers. They observed that the modes could interact and that the final stage depended on their relative initial amplitudes. For example, when the initial amplitudes of the traveling and the stationary modes were the same, the traveling modes, owing to their larger growth rates, would dominate most of the flow development. With this in mind, Corke and Knasiak [9, 10] documented a triple phase-locking between traveling and stationary cross-flow modes through cross-bicoherence (CBC) analysis of velocity time series that was the first experimental evidence of a triad resonance mechanism in this flow.

One of the more interesting recent revelations of the rotating-disk flow came from linear analysis by Lingwood [11], that indicated that traveling cross-flow modes on the rotating-disk flow are absolutely unstable past a critical Reynolds number of $R_{c_A} = 507$ (corrected from 513 [12]). The dimensionless frequency of these is in the range of $\omega_0^{c_A}$ from 50 to 60 [13]. Lingwood [11] suggested that the absolute instability was the dominant mechanism for transition. However, linear DNS simulations of Davies and Carpenter [14] concluded that the absolute instability does not produce a global mode and that linear-disturbance wave packets are dominated by the convective instability. Pier [13] showed that, if the amplitudes in the band of absolutely unstable frequencies reached a finite level, a secondary instability produced a global mode.

In our work, we use the flow over a rotating disk as a means of studying these different mechanisms for transition to turbulence that originate with the Type-1 cross-flow instability. The emphasis is on documenting the development of traveling modes and determining their role in the transition process with an eye towards either of the two mechanisms: nonlinear interactions with stationary modes, or temporal growth through the absolute instability.

2 Experimental setup and procedure

The rotating-disk facility consists of a polished aluminum disk mounted on an air-bearing with an integrated dc-motor. The dc-motor is controlled by a digital controller that takes feedback from an optical encoder on the motor shaft that produces ttl-pulses every 0.5° of rotation. The controller maintains a constant rotation speed to within 0.003%.
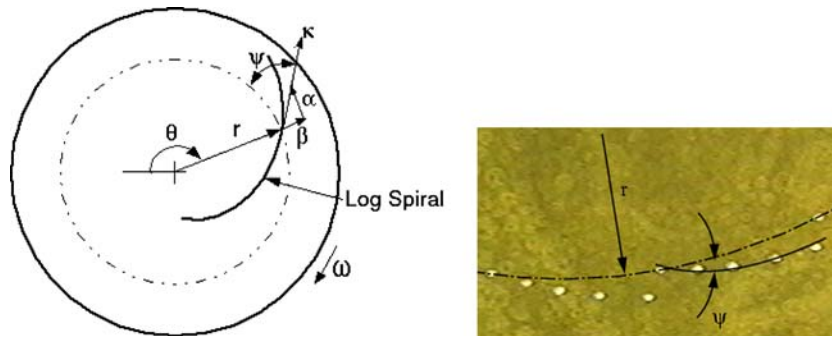
Fig. 1 Coordinate system for the rotating disk (left) and photograph of $n = 19$ spiral dot arrangement (right) used in experiment
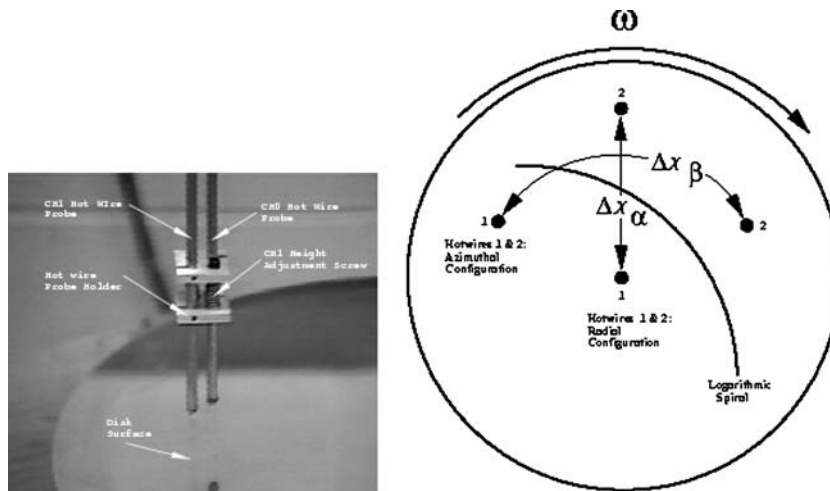

Fig. 2 Photograph of dual hot-wire probe arrangement (left) and schematic of sensor positions used in measuring wave-number vector

The aluminum disk is 45.72 cm in diameter and 3.175 cm thick. The measurement surface was ground and diamond lapped to be flat and parallel to within 0.0038 mm, and polished to a 2 micron finish.

A motorized traversing mechanism was mounted above the surface of the disk. It allowed two directions of motion: radial and wall-normal, with an accuracy of 0.0025 and 0.00025 mm, respectively. Motion was controlled through software with a digital data acquisition and control computer.

The coordinate system for the measurements on the disk is shown in the left part of Fig. 1. Either one or two hot-wire sensors were used in acquiring velocity time series in the boundary layer on the disk. The sensors were always oriented to be most sensitive to the azimuthal component of velocity, U_θ. Two simultaneous sensors were used to determine wave number vectors. Figure 2 shows a photograph of these along with a schematic of their placement for determining the separate wave numbers, α and β.

2.1 Mode-resonance setup

In an effort to better control the initial conditions, and owing to the sensitivity of this instability to surface roughness, we used an earlier technique [9, 10] and applied an array of roughness "dots" to the surface of the disk. The diameter and height of the dots were very reproducible. The diameter of the dots was 1.6 mm, and their height was 0.06 mm, which gave a dimensionless height of $h(\omega/\nu)^{1/2} = 0.16$.

Table 1 Experimental conditions and critical radii

Parameter	Value
ω	$104.7 \, \text{s}^{-1}$
ν	$1.56 \times 10^{-5} \text{m}^2/\text{s}$
R_{c_I}	285 (theory)
r_{c_I}	11.11 cm
$R_{c_{II}}$	69 [15]
$r_{c_{II}}$	2.66 cm
R_{c_A}	503 [12]
r_{c_A}	19.58 cm
r_{c_A}/r_{c_I}	1.764

The azimuthal number and spiral pattern of dots was chosen based on the azimuthal wave number that was most likely to occur naturally (that is, be most amplified based on linear theory). The scale (height and diameter) of the dots was sufficient to put energy into a narrow band of modes, but not so large that it changed the basic flow.

The case presented here corresponds to 19 spiral patterns of dots equally spaced around the disk. The spirals were located at a fixed radius band, $0.955 \leq r/r_{c_I} \leq 1.005$, where $n = 19$ was most the amplified wave number. The critical radius, r_{c_I}, is the minimum radius for Type I cross-flow mode growth based on linear theory. The physical value is given in Table 1. The spiral pattern wave angle was $\psi = 11.2°$, which is also the most amplified value. A photograph of the spiral dot pattern is shown in the right part of Fig. 1.

The dots were applied with an inking pen attached to the traverse mechanism. The dots were positioned under computer control with an angular accuracy of 0.053°. The angular locations of the dots was always referenced to the same angular position on the disk. This position also corresponded to the first point in the acquired velocity time series.

2.2 Absolute instability setup

Our objective for this part of the experiment was to minimize background disturbances with particular attention on minimizing surface imperfections in order to limit the amplitude of stationary modes and thereby provide the potential for following disturbance wave packets as close as possible to R_{c_A}. Therefore, we used a "clean" disk without the applied surface "dots" used in the other part in the experiment. We then developed a method for introducing <u>temporal</u> disturbances off of the disk surface above the boundary layer.

The disturbance generator consisted of a pulsed micro air jet that was suspended from the traversing mechanism. A photograph and schematic of the air jet is show in Fig. 3. The air exited from a hypodermic tube with a 0.203 mm inside diameter. Two computer-controlled electronic solenoid valves, one normally closed and the other normally open, were used to generate repeatable, short-duration air pulses. The full duration of the pulse corresponded to 20% of the disk rotation. The exit of the hypodermic tube was located 4 mm above the disk surface which was approximately twice the boundary layer thickness. The radial location of the pulsed air jet corresponded to $R = 311$, which was slightly outboard of R_{c_I}, and was the same location used by Lingwood [17].

2.3 Experimental conditions

The disk was operated at a fixed rotation speed, $\omega = 104.7 \, \text{s}^{-1}$. The subsequent physical values of the critical radii for the Type I cross-flow and absolute instabilities, r_{c_I} and r_{c_A}, respectively, are given in Table 1.
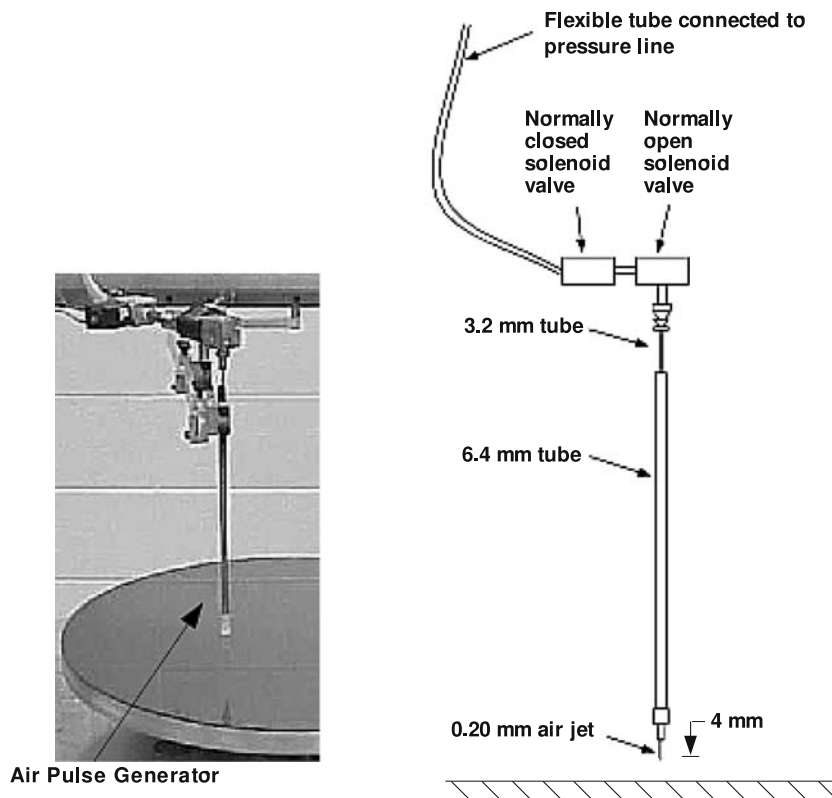
Fig. 3 Photograph and schematic of air pulse generator used to introduce temporal disturbances in boundary layer [16]

These were based on their respective critical Reynolds numbers, R_{c_I}, and R_{c_A}, the values of which are also listed in the table. For reference, the critical values of the Type II cross-flow mode is also listed.

The velocity measurements consisted of digitally sampling contiguous voltage time series points proportional to the azimuthal velocity (U_θ). With two sensors, the voltage time series were simultaneously sampled at displaced radial (r) locations for the same discrete wall-normal (z) locations over the disk. The hot-wire sensor voltages were converted to velocity through a calibration relation that was determined before making measurements.

The sampling rate was 2,500 Hz which was sufficient to resolve frequencies corresponding to traveling modes up to 1,250 Hz (well above the absolute instability range), and stationary cross-flow modes with azimuthal mode numbers (n) up to 75 ($1,250 * 2\pi/\omega$). The contiguous records were 1,024 points in length which corresponded to 6.82 revolutions of the disk. A total of 32 records were sampled at each z-position. The absolute height of the sensor at the closest position above the wall was set using a cathetometer with a resolution of 0.002 mm.

3 Results

3.1 Mode-triad resonance

Mean velocity profiles which document the basic flow are shown in Fig. 4. These have been normalized by the similarity forms and compared to the analytic solution (solid curve) for flow over an infinite rotating disk (see for example [18, p. 215]). Shown for reference as the horizontal line at the bottom of the plot is
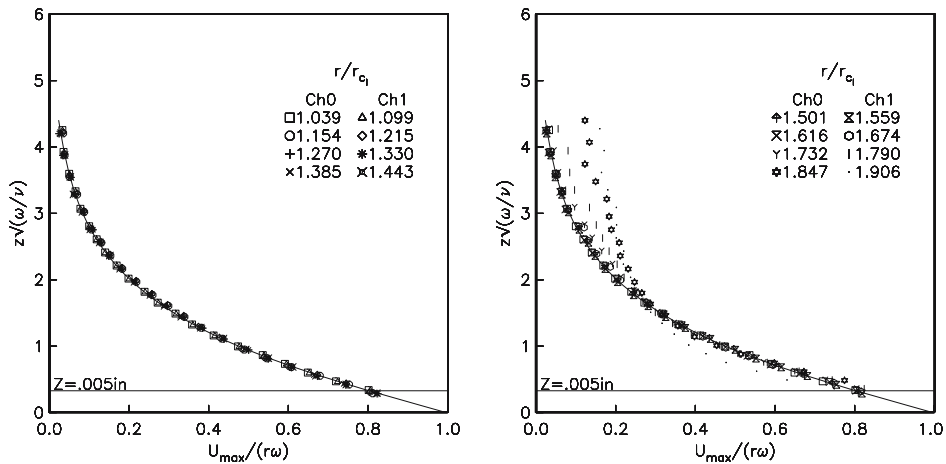
Fig. 4 Mean velocity profiles at "linear" (left) and "nonlinear" (right) radii for 19-spiral case

the height of the dots in similarity units. The left plot corresponds to the "linear range" of radial locations. The right plot to the "nonlinear range", where the mean profile deviates from the laminar distribution. The "linear range" results show excellent agreement with the theoretical profile. The mean velocity profiles only begin to deviate when the amplitude of the cross-flow modes reach sufficient level to distort the mean flow. This is observed to occur at $r/r_{c_I} \simeq 1.732$ for this case. The location depends on initial disturbance amplitudes. For a "clean" disk surface used for the studies on the absolute instability [16, 19], the location of the start of mean-flow distortion was further outboard at $r/r_{c_I} \simeq 1.89$.

The velocity fluctuations in the time series were decomposed into the contributions from stationary and traveling-instability modes following Corke and Knasiak [10]. To do this, we first constructed the rotation-averaged time series by forming ensemble averages that were triggered on a single disk location. The contribution of the traveling modes was obtained by subtracting the rotation-averaged time series from the total time series for each disk rotation. This process was performed for each of the sampled spatial locations.

The dot-spirals placed on the disk surface were intended to initially excite a narrow band of cross-flow modes to provide a well-controlled initial condition. This is demonstrated in Fig. 5 which shows spectra of azimuthal velocity fluctuations of the stationary modes from the rotation-averaged time series at different radial locations, within the linear range defined by the mean velocity profiles (Fig. 4). The first location, $r/r_{c_I} = 1.039$ is the location of the $n = 19$ dot-spirals. The spectrum shows a clear peak at $n = 19$. The vertical lines near the top of each spectrum plot indicate the most amplified stationary cross-flow mode based on linear theory. At $r/r_{c_I} = 1.039$, $n = 19$ is the most amplified. The most amplified azimuthal wave number varies as $n = \beta R$, where β is the instability wave number in the θ-direction (Fig. 1). The parameter β is nearly constant with R [20] so that n should vary nearly linearly with R. The vertical lines near the top of each spectrum plot at the different radial locations reflect this. The spectra show that the $n = 19$ mode is initially dominant but eventually the higher mode numbers grow so that the spectrum at the most outboard location, $r/r_{c_I} = 1.616$, has a broad peak approximately centered about the linear-theory's most amplified n. This broad peak represents the sum of the growing and decaying stationary cross-flow modes that have evolved to that radial location on the disk.

The right part of Fig. 5 shows the wall-normal amplitude distribution for the $n = 19$ mode close to the location of the dot-spiral. For this, $u'(\theta)$ is the r.m.s. of the azimuthal velocity fluctuations, and $U_{max} = \omega r$ is the local disk surface velocity. The purpose is to demonstrate that the amplitude distribution is similar to the linear-theory eigenfunction (dots) indicating that the dot-spiral is exciting the linear mode and that the amplitude is within the linear-theory assumptions. The agreement is acceptable.
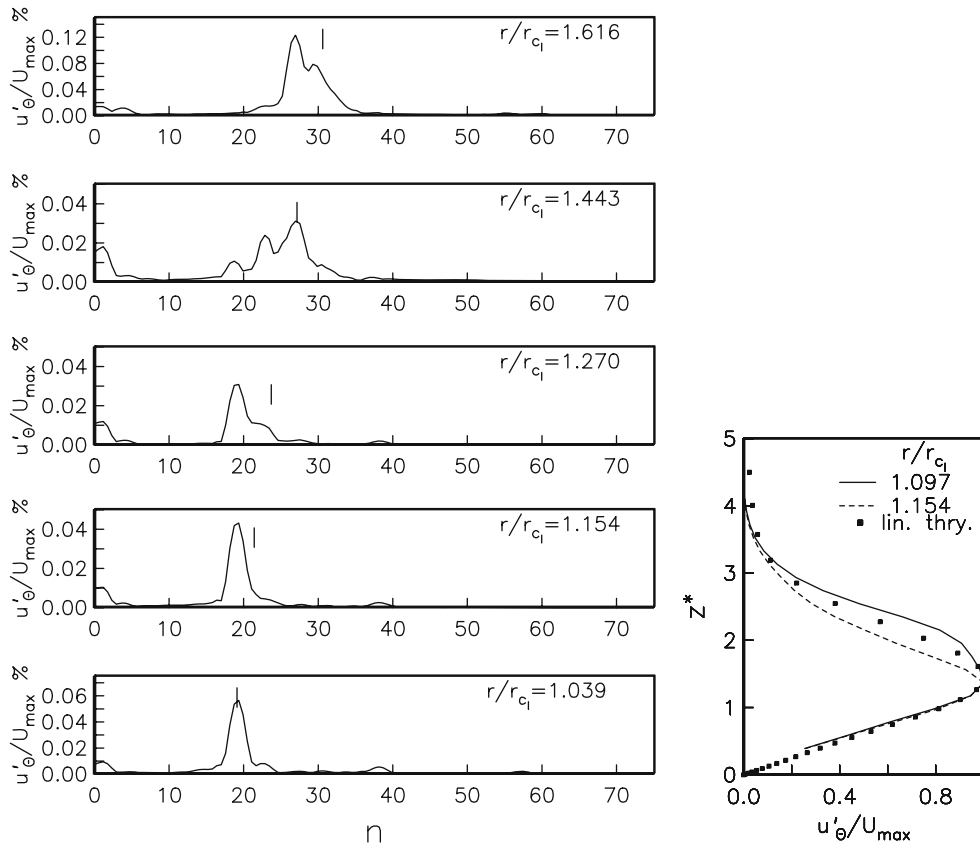
Fig. 5 Spectra of azimuthal velocity fluctuations associated with stationary modes measured at $z^* = 1.5$ for increasing radii in linear development region (left), and wall-normal amplitude distributions for $n = 19$ stationary mode close to dot-spiral location (right)

Figure 6 shows velocity spectra at radii that encompass the nonlinear development region based on the mean-flow distortion observed in the mean-velocity profiles (Fig. 4). The left group of spectra correspond to the stationary modes. The right group corresponds to traveling modes. With the stationary-mode spectra, for $r/r_{c_I} \leq 1.789$, the vertical lines mark linear most amplified values based on $n = \beta R$. The largest-amplitude spectral peaks no longer correspond to the linear most amplified. In addition, we observe a broadening of the spectra and the development of multiple discrete peaks. Accompanying this is the appearance of a peak at a low wave number near $n = 4$. For $r/r_{c_I} \geq 1.789$, the vertical lines mark $n = 4$. The spectral peak at $n = 4$ is the most dominant for $r/r_{c_I} \geq 1.9$. Beyond that location, the mean velocity profiles (Fig. 4) became fuller near the disk surface indicating that the flow was turbulent. The spectra in this region are observed to have a broad energy distribution indicative of turbulent flow.

The radial growth and decay of selected stationary modes of $n = 19$, 27 and 4 is illustrated in the left part of Fig. 7. This corresponds to the maximum amplitude of these modes measured at different radii. The amplitude axis is a log scale in order to emphasize exponential growth. First focusing on the $n = 19$ mode, its initial amplitude is larger than the others because it was initially excited by the 19 dot-spirals. The dots were placed at the radius where $n = 19$ is most amplified. Outboard of that radius, its amplitude is observed to decay exponentially, which is expected from linear theory.

The mode number $n = 27$ had the largest amplitude at the end of the linear development region. Figure 7 indicates that it started from a lower initial amplitude and grows exponentially until it reaches a maximum at $r/r_{c_I} = 1.6$.
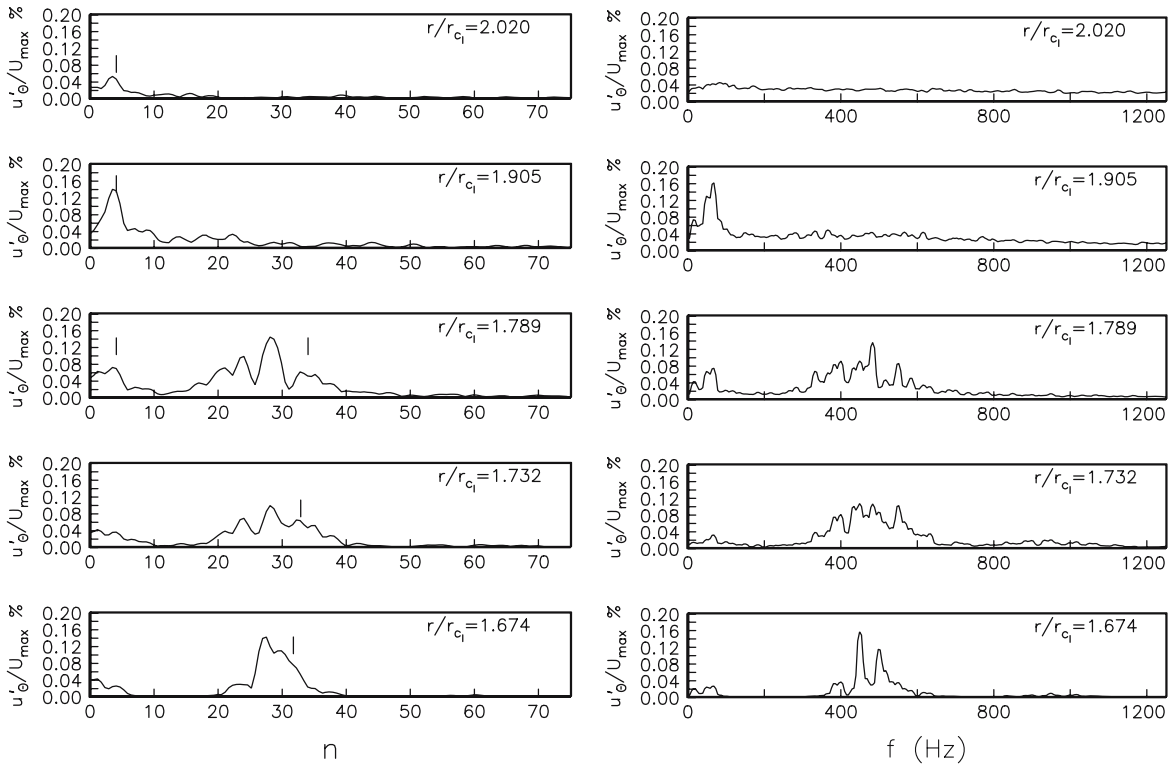
Fig. 6 Spectra of azimuthal velocity fluctuations associated with stationary modes (left) and traveling modes (right) measured at $z^* = 1.5$ for increasing radii in nonlinear development region. On stationary mode spectra, for $r/r_{c_I} \leq 1.789$ vertical lines mark linear most amplified values, and for $r/r_{c_I} \geq 1.789$ vertical lines also mark $n = 4$
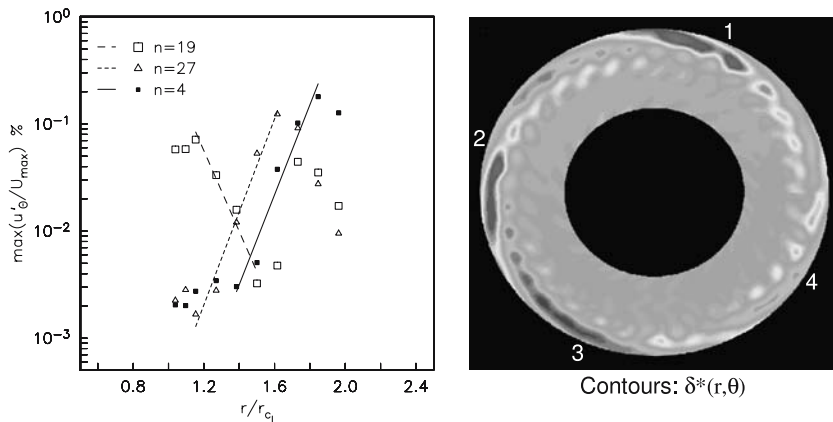

Fig. 7 Radial growth of maximum amplitude of selected stationary modes (left) and contours of boundary-layer displacement thickness (right) for 19 dot-spiral case

In the nonlinear region, the spectra for the stationary modes (left part, Fig. 6) had shown the growth of a mode at $n = 4$ that was dominant at transition. The radial growth of this mode is included in Fig. 7. This documents that the $n = 4$ mode only exhibits exponential growth at large radii ($r/r_{c_I} > 1.4$) where linear theory predicts such low-wave-number stationary modes to be highly damped. This suggests that the $n = 4$ mode growth is due to a nonlinear mechanism.
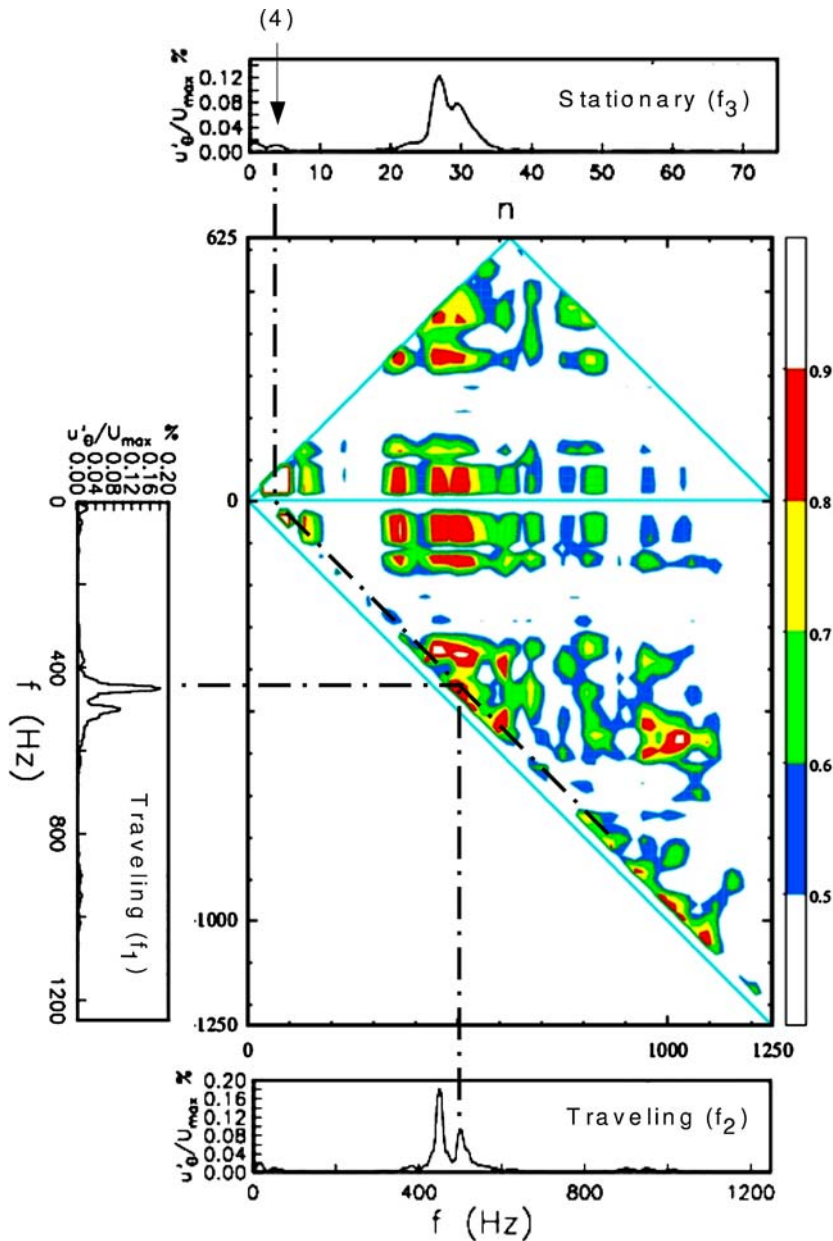
Fig. 8 Contours of cross-bicoherence between traveling modes and stationary modes at $r/r_{c_l} = 1.616$ for 19 dot-spiral case. Dashed line signifies interaction for $f_1 = 517\,\mathrm{Hz}$ and $f_2 = 449\,\mathrm{Hz}$ so that $f_1 - f_2 = 68\,\mathrm{Hz}$ which when divided by the disk frequency (16.667 Hz) gives $n = 4$

We can observe the impact of the $n = 4$ mode on transition by viewing the azimuthal variation of the displacement thickness, $\delta_*(r, \theta)/\overline{\delta_*(r)}$ in the cylindrical coordinate of the disk. This is shown in the right part of Fig. 7. This was constructed from the rotation-averaged mean velocity profiles. The displacement thickness values are shown as constant level gray-scale contours. The darker shaded regions correspond to where the displacement thickness is less than the mean. The lighter shaded regions are where it is greater than the mean. We imagine the stationary co-rotating cross-flow vortices, which form in the nonlinear region, to act like "pumps", bringing the high-momentum fluid from the wall to the outer part of the

boundary layer, and low momentum fluid towards the wall. This results in a distortion of the mean flow in which on one side of the vortex, the boundary layer will thin, and on the other side it will thicken. The $n = 4$ variation is clearly visible as the four alternating light/dark regions around the disk at the outer radii. These have been marked by numbers to guide the eye.

Corke and Knasiak [9,10] had documented the growth of a low-wavenumber ($n = 3$) stationary mode during the later stages of transition to turbulence on the disk, and speculated that it was due to a triad resonance with a pair of traveling modes. For this, they demonstrated a triple phase-locking through a cross-bicoherence (CBC) analysis, which is the first condition of proof of a triad resonance.

A CBC analysis for the present conditions is shown in Fig. 8 for the location $r/r_{c_I} = 1.616$. The CBC is a measure of phase-locking between three modes such that the ensemble averaged phase between the modes ($\theta(f_i)$) satisfies $\theta(f_1) \pm \theta(f_2) = \theta(f_{1\pm2})$. The method of calculating the cross-bicoherence followed that of Corke et al. [21].

The CBC is a normalized quantity, where CBC=1 represents perfect phase locking, and CBC$\,=0$ indicates no phase locking. The valid region of interacting frequencies forms two triangles. The upper triangle corresponds to summing interactions. The lower triangle corresponds to difference interactions. Because the CBC involve three frequencies, it requires three frequency axes. In our application, the horizontal and vertical axes corresponds to frequencies of traveling modes. The third frequency is read as a point of intersection with the horizontal axis of a line drawn parallel to the right side of the upper triangle or left side of the lower triangle. Here, the third axis refers to frequencies of stationary modes so that it can be divided by the disk-rotation frequency (16.667 Hz) to obtain the azimuthal mode number n. The CBC-levels are drawn as filled contours, with the contour scale shown on the right edge of the plot. We are only showing the most significant CBC levels (> 0.5). For reference, spectra for the traveling and stationary disturbances are shown along their respective axis edges.

The dashed lines highlight one example of a difference interaction between two dominant frequencies in the spectrum of traveling modes and the $n = 4$ stationary mode. This corresponds to $f_1 = 517$ Hz and $f_2 = 449$ Hz so that $f_1 - f_2 = 68$ Hz which when divided by the disk frequency (16.667 Hz) gives $n = 4$.

The CBC indicate phase-locking that is the first evidence of a triad resonance between pairs of traveling cross-flow modes and low-mode-number stationary modes that can lead to the nonlinear growth of the $n = 4$ mode at transition. The following section investigates the second condition which is wavenumber matching between the three modes.

3.2 Dispersion relation—stationary modes

A spatial correlation analysis of time series corresponding to the stationary modes was conducted using the cross-correlation between the two simultaneous hot-wire sensors to determine the two-dimensional wavenumber vector, κ at each frequency. As defined in Fig. 1, the wave vector κ is a function of the radial and azimuthal wave numbers α and β, which define the spiral wave angle, $\psi = \arctan(\beta/\alpha)$.

Dispersion curves for β are presented in the left part of Fig. 9. The stationary dispersion curves are used as a check on the accuracy of the wave-number measurements. Because the rotation ensemble-averaged flow is a priori stationary, its phase speed is exactly that of the disk. The results verified the expected dispersion relation, $n = \beta R$.

Dispersion curves were also determined for the radial mode number α. These were used along with those for β, to determine the spiral angle ψ of the instability wave angle, $\psi = \tan^{-1}(\beta/\alpha)$. These are presented in the right part of Fig. 9. This verifies that the stationary modes in this case follow the theoretically preferred angle of 11.2°, shown by the solid line.
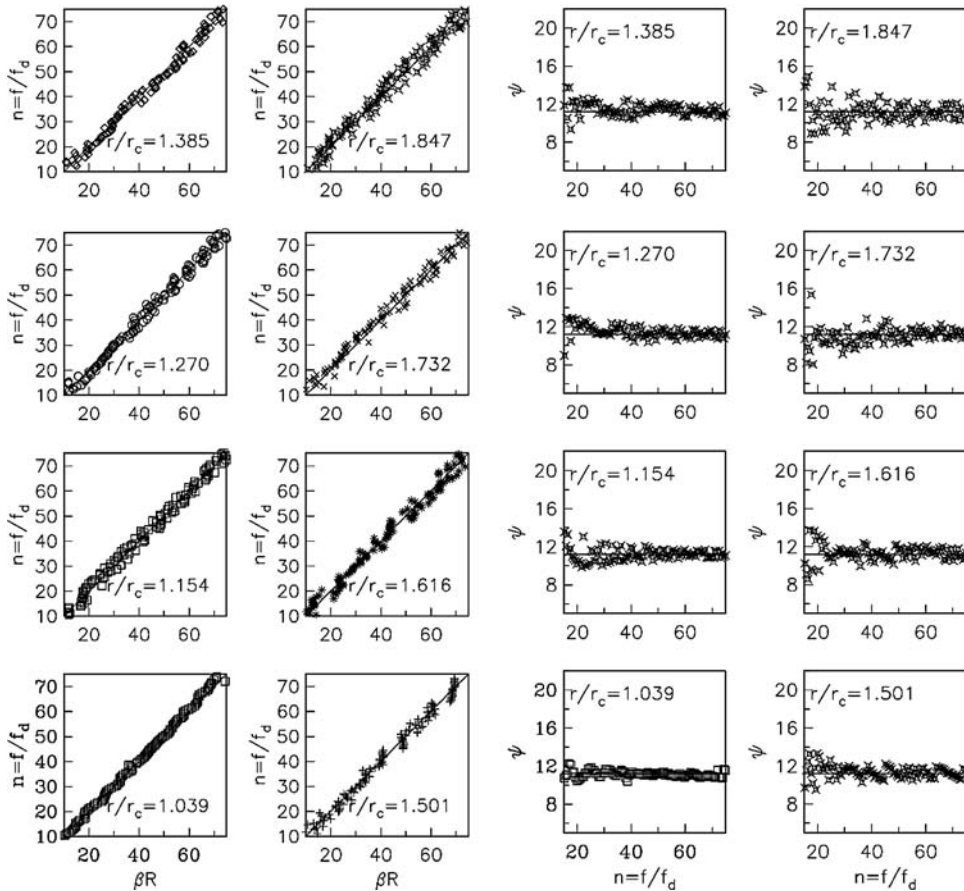
Fig. 9 Stationary mode dispersion curves for β (left) and stationary mode spiral wave angles, ψ (right) at different radial locations for 19-spiral case

3.3 Dispersion relation—traveling modes

The dispersion curves for β for the traveling modes are shown in the left part of Fig. 10. In the linear region, the values are very close to falling on the $45°$ line, indicating wave speeds that are close to the disk speed. However, in the nonlinear region, starting at $r/r_{c_I} = 1.501$, we observe a change in the slope of the dispersion curve whereby wave numbers, $\beta R \leq 25$ are traveling significantly faster than the disk speed, and $\beta R > 25$ are traveling significantly slower. The radial wavenumber dispersion for the traveling modes were found to vary linearly with Reynolds number so that the change in β resulted in a change in the wave angles of the traveling modes in the nonlinear region. This is documented in the right part of Fig. 10. In the linear region, the spiral wave angle of the traveling modes is the same as the stationary modes. However, in the nonlinear region, lower frequencies ($f/f_d \leq 25$) have lower wave angles than those of the stationary modes, and higher frequencies ($f/f_d > 25$) have wave angles that are larger than those of the stationary modes. Higher wave angles signify that these waves are spiraling outward faster than the stationary modes.

We can observe evidence of traveling modes that develop higher wave angles than those of stationary modes in flow visualization by Wilkinson et al. [22]. An example is shown in Fig. 11. This shows the visualized flow over a rotating disk obtained using a smoke wire located at the line $\overline{OW}$, where O marks the center of the disk. An orifice through the disk was used to introduce a time-dependent disturbance. The line $\overline{OF}$ locates the oriface relative to the fixed smoke wire at the time that a light flash was activated to
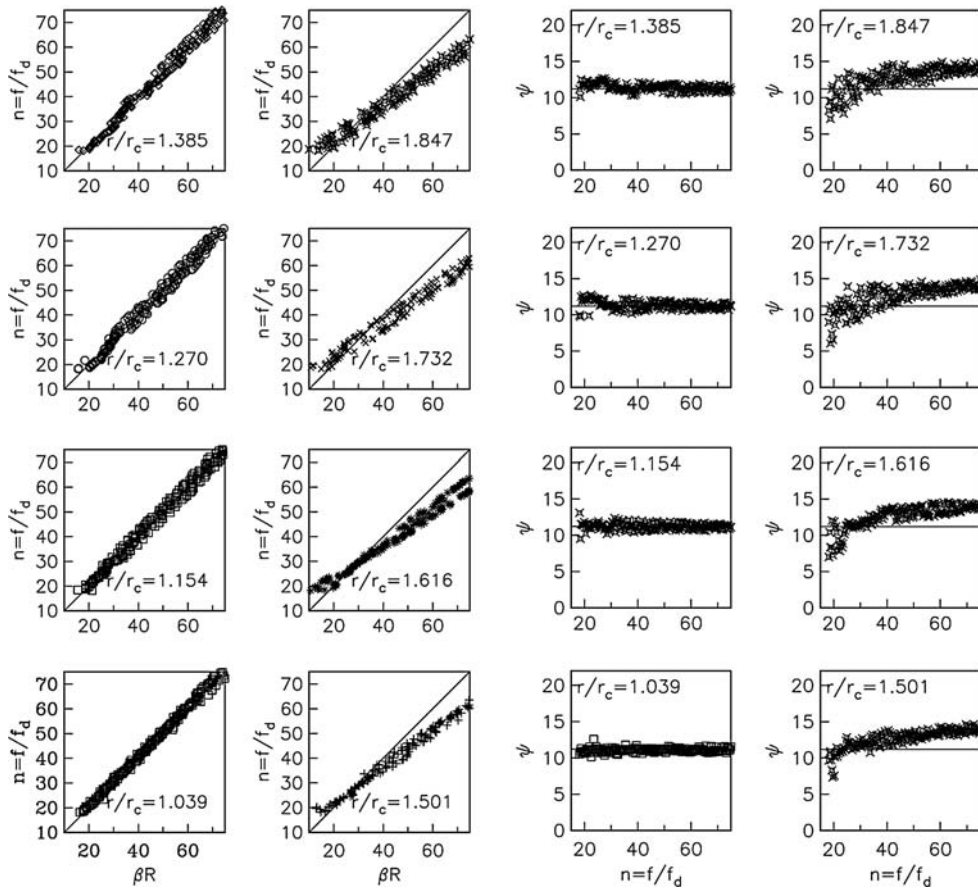
Fig. 10 Traveling-mode dispersion curves for β (left) and traveling-mode spiral wave angles, ψ (right) at different radial locations for 19-spiral case

take the smoke image. The dashed line $\overline{OP}$ locates the oriface at the time a suction pulse was delivered to it. The disk is rotating counter-clockwise in the image. The arc, r_h is the physical trajectory of the oriface. The flow visualization reveals two features. The first is a stationary wave (log-spiral) that is due to the hole in the surface. This was the reason that we used a disturbance generator above the surface of the disk. The other feature is the unsteady waves that were generated by an unsteady air pulse at the site of the hole. We have selected one of the waves and drawn a tangent vector which represents the wave vector κ. The inside angle between this vector and a constant radius arc represents the wave angle, ψ (see left schematic in Fig. 1). It is clear that the wave angle of this unsteady wave is larger than that of the stationary wave produced by the oriface at that azimuthal location, denoted by r. Therefore, the traveling wave has a larger spiral angle than the stationary wave at that radius, which supports our dispersion measurement results.

3.4 Triad wavenumber resonance

The final step in verifying the triad resonance is to show that frequencies that were found to have a significant CBC also satisfied a triple wave number matching namely, $\kappa_2 \pm \kappa_1 = \kappa_3$, where $\kappa_i = (\alpha_i^2 + \beta_i^2)^{1/2}$. An example for the interaction indicated by the dashed lines in the CBC in Fig. 8 are presented in Table 2. The first two columns list the frequencies of traveling modes whose difference frequency when divided by the disk-rotation frequency, listed in column 3, was 4 (± 0.1 based on the spectral analysis Δf). Columns 4

Fig. 11 Visualization of flow over disk surface with a surface hole used to introduce an unsteady disturbance. From Wilkinson et al. [22] (with permission)
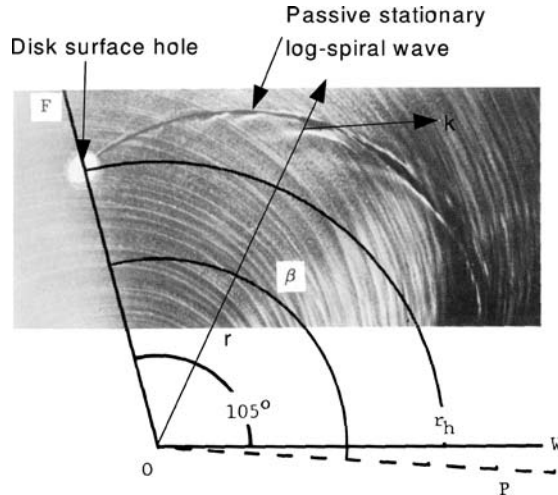

Table 2 Triad frequency and wavenumber matching for difference interaction leading to stationary $n = 4$ mode, $r/r_{c_I} = 1.616$, $f_d = 16.667$ Hz. 19-spiral case

Traveling		Stationary	Traveling		Stationary	
f_2 (Hz)	f_1 (Hz)	$n = (f_2 - f_1)/f_d$	κ_2	κ_1	κ_3	$(\kappa_2 - \kappa_1)/\kappa_3$
517.3	449.0	4	22.73	19.61	3.12	1.04
527.1	458.8	4	23.17	20.06	3.12	1.04
537.0	468.5	4	23.62	20.50	3.12	1.04
546.6	478.3	4	24.05	20.95	3.10	1.03
556.4	488.1	4	24.50	21.39	3.10	1.03
566.1	497.8	4	24.94	21.84	3.10	1.03
575.9	507.6	4	25.39	22.28	3.10	1.03

and 5 list the wave-number vectors for the respective frequencies f_2 and f_1, in columns 1 and 2. The wave number of the $n = 4$ stationary mode, κ_3, is listed in column 6. The degree to which this matches $\kappa_2 - \kappa_1$ is listed as the ratio $(\kappa_2 - \kappa_1)/\kappa_3$ in column 7. A perfect wave-number matching has the ratio of 1. The absolute uncertainty in the wavenumber vector is largest at the lower frequencies, and therefore affects the result for the low wavenumber (4) the most. Therefore, a 4% error is considered excellent.

The measured wave-number matching ratio, $(\kappa_2 - \kappa_1)/\kappa_3$, for all of the possible sum-and-difference interactions at $r/r_{c_I} = 1.616$ are presented in Fig. 12. The ratio is plotted as constant level contours in the format of the CBC that were presented in Fig. 8. Only contour levels corresponding to error levels less than 5% are shown.

The dashed line shows the same triple-frequency interaction with the $n = 4$ mode that was highlighted in the previous CBC. We observe that the dashed line in the lower triangle falls on the thin band in which the wave number matching is nearly perfect. These interactions are part of those listed in Table 2. There are obviously many other difference-and-summed frequency interactions that also satisfy the wave-number matching criterion for triad resonance. We can conclude from this that there is a strong nonlinear coupling between the traveling and stationary cross-flow modes that is distributing energy throughout the spectrum in the stage leading to turbulence. In terms of energy, the $n = 4$ mode is dominant in the spectrum.
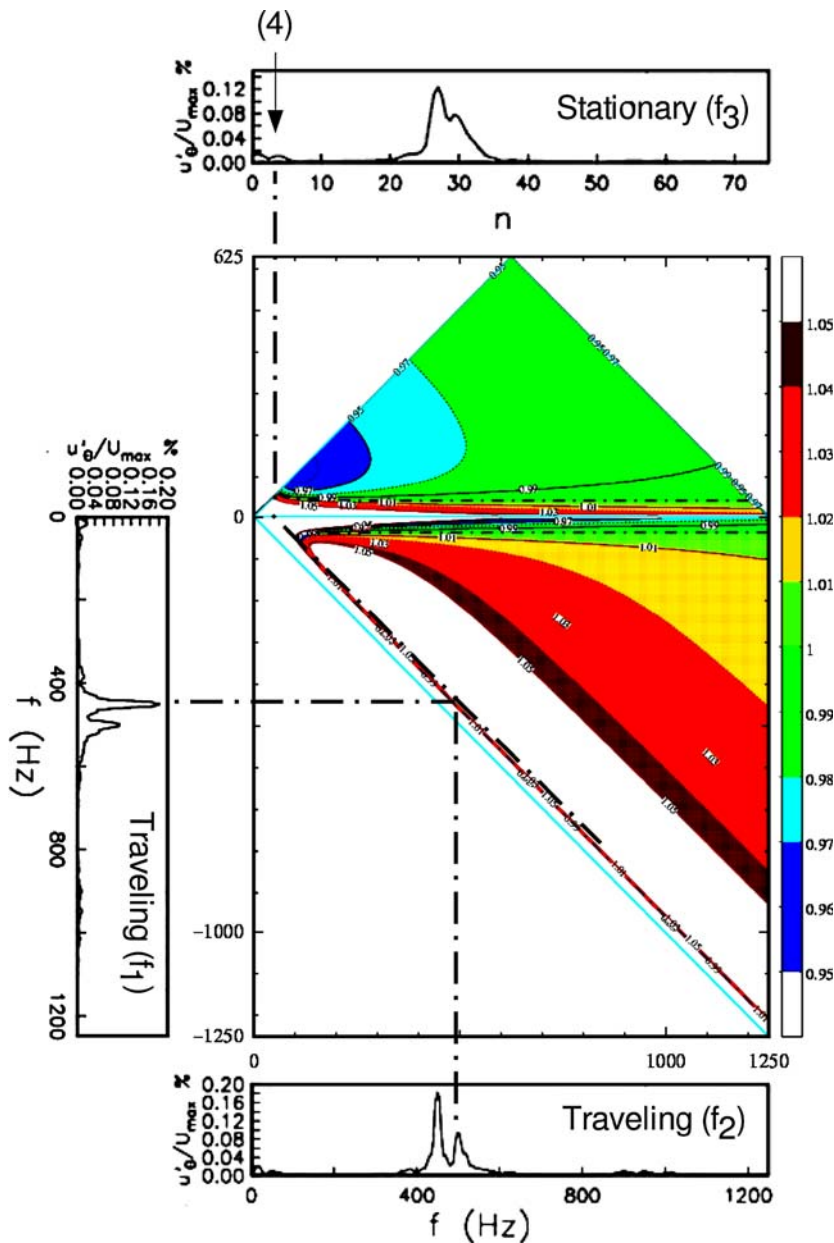
Fig. 12 Contours of wave-number matching error, $(\kappa_2 - \kappa_1)/\kappa_3$, between traveling modes and stationary modes at $r/r_{c_l} = 1.616$ for 19 dot-spiral case. Dashed line signifies interaction for $f_1 = 517$ Hz and $f_2 = 449$ Hz so that $f_1 - f_2 = 68$ Hz which when divided by the disk frequency (16.667 Hz) gives $n = 4$

4 Role of absolute instability

The previous results only considered the development and nonlinear interaction of spatial convective modes. The discovery of the linear absolute instability mechanism led Lingwood [11] to suggest that this was the dominant mechanism for transition. This led us [16, 19] to investigate the growth of controlled temporal disturbances. As described in Sect. 2, the boundary layer was perturbed by short-duration pulses of air from a small-diameter suspended air jet. This led to the growth of disturbance wave packets. Spectral

analysis of the wave packets indicated that their initial frequency content, growth rate and wall-normal amplitude distributions were consistent with linear theory [16, 19], thereby satisfying the assumptions of Lingwood analysis and linear DNS simulations of Davies and Carpenter [14]. The experiment was performed on a smooth disk, without the applied "dots", and special care was taken to clean the disk of any minute dust particles that would produce uncontrolled conditions. As a result, the Reynolds number where mean-flow distortion was first observed was 539 ($r/r_{c_I} = 1.89$) versus 493 in the case previously described with the 19 dot-spirals. On the smooth disk, this was 6% beyond R_{c_A} which hints that the absolute instability mechanism was not the dominant factor.

An example of the wave packets produced in the experiment are shown in Fig. 13. These were ensemble averages triggered on the air pulse not on the disk position so that they represent only traveling modes. The wave packets were measured at one radial location corresponding to $r/r_{c_A} = 1.01$, and different azimuthal locations relative to the pulse generator to mark temporal development.

The linear absolute instability theory specifies that traveling cross-flow modes with a frequency of $\omega_0^{c_A} = 50$ are most amplified at R_{c_A}[13]. For our disk rotation frequency, this corresponds to a physical frequency of 833 Hz. The most amplified frequencies of traveling modes from linear theory are somewhat lower at approximately 530 Hz. This is the range of frequencies we observed in the spectra in the right part of Fig. 6. It was important to verify that energy in the wave packets included the band of the absolute instability. To document this, velocity spectra were computed for the wave packets over the full (r, θ) space of the disk. The amplitudes of two frequencies at 530, representing the initial linear band, and 1,000 Hz, representing the absolutely unstable band, were then tracked along a log-spiral emanating from the disturbance generator with a local wave angle of $\psi = 11.1°$. This wave angle had been verified by the measured dispersion curves in Fig. 10. The results are plotted in Fig. 14. The solid line corresponds to exponential fits, with the exponents corresponding to $-\alpha_i/R_{c_I}$ listed in the figure.

The results in Fig. 14 confirm that at least up to R_{c_A} (dashed vertical line), the two frequencies representing the initial linear and absolute instability bands contained energy and were growing exponentially. It was therefore a fair test of the absolute instability mechanism.

Of particular interest with the absolute instability mechanism is the spreading of the wave packets in time. This has been measured by analyzing the evolution of wave packets at all of the (r, θ) locations in which leading and trailing edges were identifiable. Where these were identifiable, the process for determining the edges of the wave packet was to use the amplitude envelope calculated from the Hilbert transform, locate the peak in the envelope amplitude, then move forward and backwards in time to find the point where the amplitude envelope reached the background level. The background level was computed for each ensemble average between $3 \leq t/T \leq 4$, where T is the time for one disk rotation.

The result of determining the wave packet leading and trailing edges is presented in Fig. 15. The squares mark all of the leading edges of the wave packets at every position. The triangles mark all of the trailing edges. The distance between the leading- and trailing-edge pairs represent individual wave packets. Singly they might appear as "fingers" that are elongated in the r-direction and slightly inclined in the time-direction. A good example of this is shown in [17, Figure 15a]. As the wave packets develop radially, they merge together. Therefore, what is ultimately important is the upper bound in time of the trailing edges and the lower bound in time of the leading edges. For reference, the solid curves mark the bounds drawn by Lingwood [17]. The dotted curve corresponds to the space–time development of the disturbance wave packet trailing edge in the linear simulation of Davies and Carpenter [14]. The vertical dashed line marks R_{c_A}.

The important aspect in Fig. 15 is with the development of the disturbance packet trailing edge near R_{c_A}. As R_{c_A} is approached, we would expect an acceleration of the temporal spreading of the wave-packet trailing edge. However, instead we observe a deceleration which asymptotically approaches a constant. The same behavior was observed by Davies and Carpenter [14] in their linear DNS simulation. Their conclusion was that although the higher frequencies are absolutely unstable, the mechanism does not produce a global mode and they were still dominated by the convective instability.
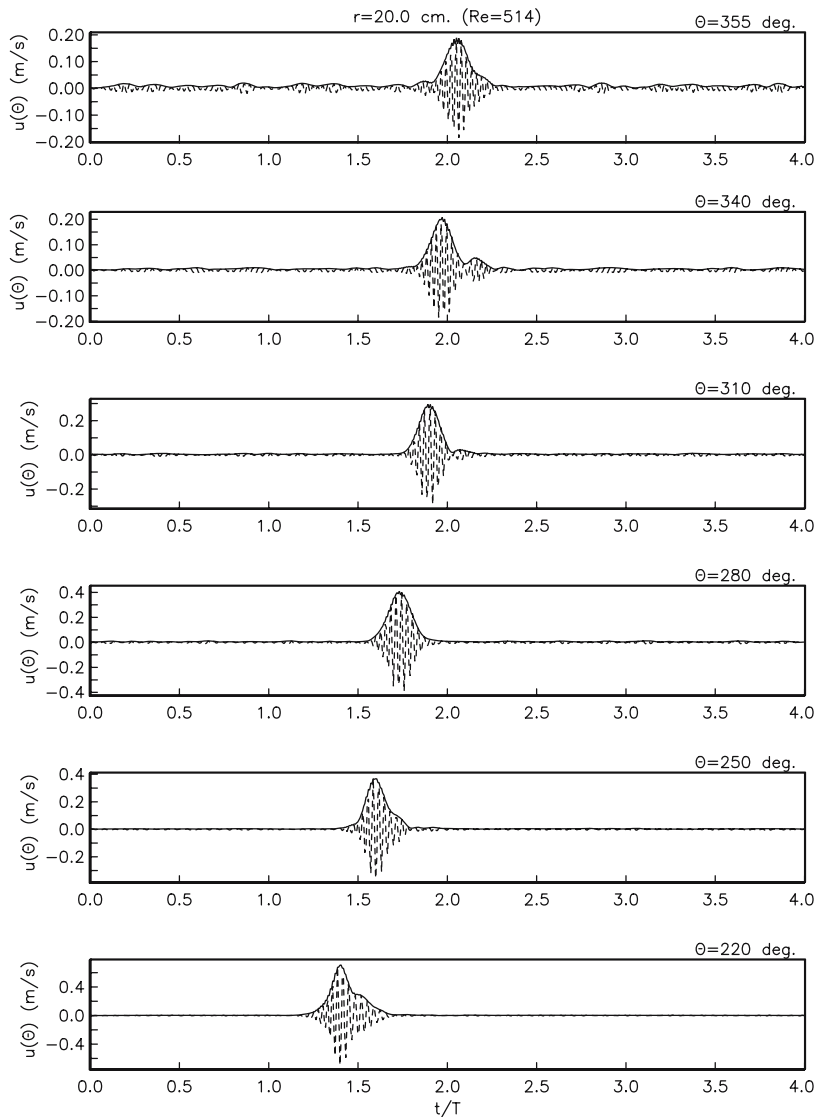
Fig. 13 Ensemble-averaged azimuthal velocity time series measured at different azimuthal angles from the pulse generator at a fixed radius of $r/r_{c_A} = 1.01$. Dashed curve is ensemble-averaged velocity triggered on air pulse. Solid curve is amplitude envelope produced by a digital Hilbert filter of our design

5 Discussion and conclusions

The principal objective of our research has been to better understand the mechanisms of transition to turbulence in the boundary layer over a rotating disk. These fell on two basic scenarios:

1. a triad resonance between pairs of traveling cross-flow modes and low-wave-number stationary modes, and
2. the absolute instability of traveling cross-flow modes.

In the study of the triad resonance mechanism, we followed the lead of Corke and Knasiak [9,10] and applied an array of roughness "dots" onto the surface of the disk to prescribe a repeatable initial condition on amplitude and wave number while otherwise not altering the mean flow. The case reported was designed
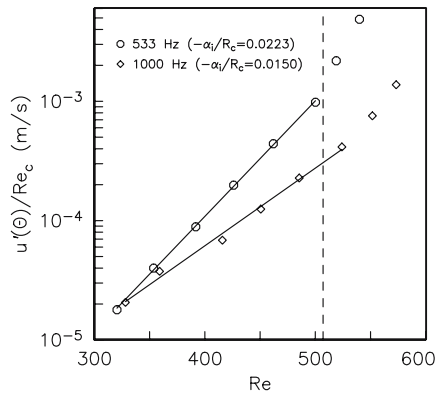
Fig. 14 Spatial development of the amplitudes of selected frequencies representing initial linear band and absolutely unstable band. Lines correspond to an exponential fits
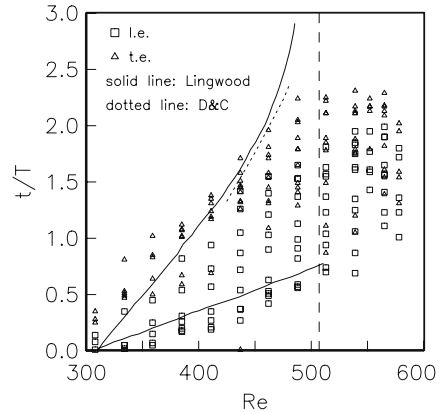
Fig. 15 Space–time map of leading and trailing edge locations of disturbance wave packets produced by jet pulse at $R = 311$. Solid curves are trend from [17]. Dashed line is from linear simulation of Davies and Carpenter [14]

to excite the mode with $n = 19$ at its most unstable radius just beyond R_{c_I}. Other cases designed to excite $n = 27$ at its most amplified radius [23], and "clean" disks [9, 10], have also been studied in this regard. Even when care is taken to wipe the disk surface, the "clean" disk is not necessarily controlled since the cross-flow instability is exceedingly sensitive to even minute dust particles, which of course is the basis behind adding dots on the surface.

A guiding precept in the linear regime was that the azimuthal mode number of stationary cross-flow modes, n, would vary according to $n = \beta R$. This was substantiated by the measured wave-number dispersion curves. Within the linear regime the largest spectral amplitudes generally coincided with the most-amplified linear mode. At any radius, a relatively broad and smooth spectral peak was observed reflecting a band of growing and decaying cross-flow modes. This changed at the onset of the nonlinear regime. We determined that nonlinear fluctuation amplitudes were reached when the mean velocity profiles first deviated from the theoretical laminar mean profiles. For the 19-spiral case this occurred at $R = 493$.

In the nonlinear region, the velocity spectra took on a multi-peaked character that coincided with the emergence of energy in low-wavenumber stationary modes. This was true in all the cases with or without the applied dots, although the discrete mode numbers varied. For the 19 dot-spirals reported here, the dominant mode was at $n = 4$. A 27-dot case [23] had $n = 5$. A previous "clean" case [10] also observed $n = 4$ to be dominant.

The amplitude of the $n = 4$ mode was found to grow only in the nonlinear region when the most amplified linear mode growth had saturated. From the onset of its growth, its wall-normal amplitude distribution was two-peaked [23]. From these two characteristics, we deduced that it was a nonlinear mode.

The CBC between time series that had been decomposed into stationary and traveling types confirmed a significant phase-locking. This occurred through difference interactions, at first involving the largest-amplitude traveling mode, and a side-band mode. Because the amplitudes of the traveling modes were larger than the $n = 4$ mode, and the stationary mode was only found to grow in the nonlinear region, we expect that energy was transferred from the traveling modes to the stationary mode.

With increasing Reynolds number, the number of traveling modes that exhibited high CBC level with the $n = 4$ mode increased. This is due in part to the natural shift in the most amplified band to higher frequencies with increasing radii (Reynolds numbers). Well into the nonlinear region, other interactions which involved higher-mode-number stationary modes were found to occur [23]. These accounted for the multi-peaked character that the stationary-mode spectrum developed in the nonlinear region.

The final step in verifying the triad resonance was to show that frequencies that were found to have a significant CBC also satisfied a triple wave-number matching namely, $\kappa_2 \pm \kappa_1 = \kappa_3$, where $\kappa_i = (\alpha_i^2 + \beta_i^2)^{1/2}$. The measurement of the wave-number vectors involved correlating the time series from two simultaneously sampled sensors placed a close distance apart.

The dispersion curves for the stationary modes effectively confirmed the accuracy of the wave-number measurements, giving phase speeds that were exactly that of the disk. These results also verified the dispersion relation, $n = \beta R$, where $\beta = 0.0698$ [20]. The measurements of the azimuthal wave number, α of the stationary modes agreed with the linear-theory predictions of the most amplified (0.354) and therefore agreed with the theoretically preferred spiral wave angle of 11.2°.

The dispersion curves for the traveling modes showed different characteristics between the linear and nonlinear regimes. In the linear region, the dispersion curve for β indicated phase speeds for all mode numbers that were close to the disk speed. This sharply changed in the nonlinear region where lower wave numbers ($\beta R \leq 25$) began to move faster than the disk, and higher wave numbers moved significantly slower than the disk. The result was that the spiral angle of lower mode numbers reduced, while those of the higher mode numbers increased. The significance of this on the triad resonance mechanism is not known.

A wave-number matching ratio, $(\kappa_2 - \kappa_1)/\kappa_3$, for all of the possible sum and difference frequency combinations between pairs of traveling modes and a stationary mode revealed abundant interactions that satisfied the triad resonance condition. This confirmed that the $n = 4$ mode resulted from this mechanism, and that it could lead to rapid spectral filling.

In contrast to the triad resonance mechanism, the absolute instability mechanism was not nearly as dominant. Conditions were set that assured that the amplitudes of the absolutely unstable frequency band were linear in order to match the theory. Being well above the most-amplified convective-instability frequencies, their amplitudes were generally lower approaching R_{c_A}. Nonetheless, the amplitudes in the absolutely unstable band were measurable and growing linearly.

Although wave packets made up of a spectrum that included the most amplified convective and absolutely unstable frequencies initially showed some temporal spreading, they never achieved an expansive temporal growth that might account for a sharp transition front speculated as experimental evidence of the mechanism [11]. This, in fact, was consistent with linear DNS simulations [14] that indicated the linear absolute-instability mechanism does not lead to a global mode, and the short-term temporal growth is dominated by the convective instabilities.

Fig. 16 Visualization image of flow over rotating disk from Kobayashi et al. [4]. Numbers denote our conjecture of low-azimuthal-wave-number features that are associated with triad resonance mechanism
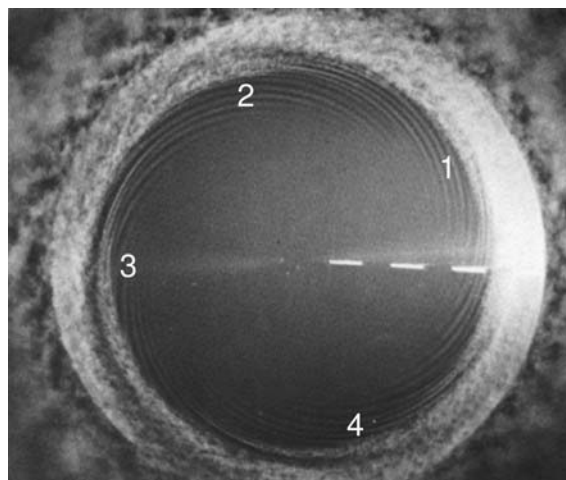
Since flow visualization was cited as possible evidence of the role of the linear absolute instability on transition to turbulence, can we find similar evidence of the triad resonance mechanism? One of the most cited and beautiful flow visualization images for the rotating disk is that of Kobayashi et al. [4]. This has been reproduced in Fig. 16. Although this image has previously been used to demonstrate a sharp transition front, closer inspection reveals a large-azimuthal wave-length variation that we have taken the liberty to number (1–4). We note the similar character of this to the displacement-thickness variation that was presented in the right part of Fig. 7. One could argue that there are as few as 3 or as many as 5. However, these features are consistent with the triad resonance mechanism that leads to the dominant growth of the low-wavenumber stationary mode, as well as a filling of the spectrum accompanying transition to turbulence. Being a nonlinear mechanism, this would also account for a rather sharp transition front of the fine scales that was thought to be evidence of the linear absolute instability. However, being a convective-instability mechanism, the exact location of where transition occurs will depend on the initial conditions that govern disturbance amplitudes. This is, in fact, more consistent with quantitative measurements that reveal considerable variation in transition Reynolds numbers, with the average for a "clean" disk being about 8% higher than the absolute-instability critical Reynolds number [6].

References

1. Smith N (1946) Exploratory investigation of laminar boundary layer oscillations on a rotating disk. NACA TN-1227
2. Gregory N, Stuart J, Walker W (1955) On the stability of three-dimensional boundary layers with applications to the flow due to a rotating disk. Phil Trans Roy Soc London Ser. A, 248:155–199
3. Federov B, Plavnik G, Prokhorov I, Zhukhovitskii L (1976) Study of a transient flow regime on a rotating disk. J Eng Phys 31:1060–1068
4. Kobayashi R, Kohama Y, Takamadate Ch (1980) Spiral vortices in boundary layer transition regime on a rotating disk. Acta Mech 35:71–82
5. Kohama Y (1984) Study on boundary layer transition of a rotating disk. Acta Mech 50:193–199
6. Wilkinson S, Malik M (1985) Stability experiments in the flow over a rotating disk. AIAA J 23:588–595
7. Lekoudis S (1980) Resonant wave interactions on a swept wing. AIAA J 18(1):122–124
8. Malik M, Li F, Chang C-L (1994) Crossflow disturbances in three-dimensional boundary layers: nonlinear development, wave interaction & secondary instability. J Fluid Mech 268:1–36
9. Corke TC, Knasiak KF (1994) Cross-flow instability with periodic distributed roughness. Transition, turbulence & combustion, vol I. Kluwer Acad. Pub., pp 43–62
10. Corke TC, Knasiak KF (1998) Stationary-traveling cross-flow mode interactions on a rotating disk. J Fluid Mech 355:285–315
11. Lingwood RJ (1995) An experimental study of absolute instability of the rotating-disk boundary layer flow. J Fluid Mech 314:373–405
12. Lingwood RJ (1997) On the effect of suction and injection on the absolute instability of the rotating-disk boundary layer. Phys Fluids 9:1317–1328
13. Pier B (2003) Finite-amplitude crossflow vortices, secondary instability and transition in the rotating-disk boundary layer. J Fluid Mech 487:315–343
14. Davies C, Carpenter PW (2003) Global behaviour corresponding to the absolute instability of the rotating-disk boundary layer. J Fluid Mech 486:287–329
15. Faller AJ (1991) Instability and transition of disturbed flow over a rotating disk. J Fluid Mech 230:245–269
16. Othman H (2005) Experimental study of absolute instability over a rotating disk, Ph.D. Thesis, University of Notre Dame, Aerospace and Mechanical Engineering Department, Notre Dame, IN
17. Lingwood RJ (1996) An experimental study of absolute instability of the rotating-disk boundary-layer flow. J Fluid Mech 314:373–405
18. Schlichting H (1968) Boundary layer theory, 6th ed. Mc-Graw-Hill, New York, NY
19. Othman H, Corke T (2006) Experimental investigation of absolute instability of a rotating-disk boundary layer. J Fluid Mech (to appear)
20. Malik M, Wilkinson S, Orszag S (1981) Instability and transition in rotating disk flow. AIAA J 19(9):1131–1138

21. Corke TC, Shakib F, Nagib H (1991) Mode selection and resonant phase locking in unstable jets. J Fluid Mech 223:253–311
22. Wilkinson S, Blachard A, Gaster M, Tritz T, Gad-el-Hak M, Selby G (1989) Flow visualization of a wave packet on a rotating disk, instability and transition, vol 1. Springer-Verlag, pp 306–318
23. Matlis EH (1997) Wavenumber analysis and resonance of stationary and traveling cross-flow modes on a rotating disk. M.S. Thesis, Ill. Inst. Tech., Chicago, IL, USA